Advanced Composites and Hybrid Materials (2024) 7:145
https://doi.org/10.1007/s42114-024-00957-9

RESEARCH

A novel bio-template strategy of assembled silver nanowires with cluster-random structure via tomato epidermis for transparent electromagnetic interference shielding and joule heating

Zhongmei Xia[1] · Longlong Tian[1] · Tianyi Zhang[1] · Bin Tian[1] · Fuhua Hou[1] · Ashraf Y. Elnaggar[2] · Salah M. El-Bahy[3] · Xiaojing Wang[4] · Yanlai Wang[1] · Tiantian Li[1] · Zeinhom M. El-Bahy[5]

Received: 2 June 2024 / Revised: 2 September 2024 / Accepted: 11 September 2024

Abstract

Transparent conductors (TCs) are applied in electromagnetic interference shielding and transparent electronic heaters due to their superior optoelectronic performance. Herein, a bio-template-based self-assembly strategy for silver nanowires (AgNWs) is employed to create novel "island-like" AgNW cluster morphologies, distinguishing from traditional random or circular shapes of AgNWs on PEN substrate. The unique structure ensures multidimensional pathways for free electron migration while concentrating visible light channels. Utilizing ultrasonic spray coating, AgNW random networks cover the clusters, bridge inter-cluster gaps, and ensure outstanding optoelectronic performance. Employing patterned self-assembled AgNWs combined with random networks marks a pioneering approach to achieving precise tunable electromagnetic interference shielding efficiency (EMI SE) in the X-band and optical transmittance, accommodating the diverse needs of various environments. The composite structure, featuring bottomed AgNW clusters and topped AgNW random networks (CRS), displays high transmittance with single-layer coating, achieving a remarkable figure of merit (FoM) of 15,481 (T@550 nm = 99.90%, Rs = 25.26 Ω/sq). This configuration also provides EMI shielding of 20.04 dB in the X-band, meeting commercial standards. Additional layers enhance the CRS films' optoelectronic stability accompanied by tunable EMI shielding and excellent Joule heating performance.

Keywords Transparent conductors · Bio-template · AgNW clusters · Electromagnetic interference shielding · Joule heating

✉ Xiaojing Wang
wxj@just.edu.cn

✉ Yanlai Wang
wangyanlai1978@163.com

✉ Tiantian Li
ttli@imu.edu.cn

[1] The Key Laboratory of Semiconductor Photovoltaic Technology at Universities of Inner Mongolia Autonomous Region, School of Physical Science and Technology, Inner Mongolia University, Hohhot 010021, China

[2] Department of Food Sciences and Nutrition, College of Science, Taif University, P.O. Box 11099, 21944 Taif, Saudi Arabia

[3] Department of Chemistry, Turabah University College, Taif University, P.O. Box 11099, 21944 Taif, Saudi Arabia

[4] College of Materials Science and Engineering, Jiangsu University of Science and Technology, Zhenjiang 212003, China

[5] Department of Chemistry, Faculty of Science, Al-Azhar University, Nasr City 11884, Cairo, Egypt

1 Introduction

Transparent conductors (TCs) have demonstrated significant application potential in electromagnetic interference (EMI) shielding and electronic heating [1]. Indium tin oxide (ITO) has been extensively utilized due to its superior conductivity and transparency; however, its brittleness and inadequate mechanical performance restrict its application in flexible and bendable devices [2]. In search of alternatives, researchers have explored materials such as doped zinc oxide (AZO), graphene [3], and 2D conductive materials like MXene [4], each offering unique benefits. Among these, silver nanowires (AgNWs) stand out for their outstanding electrical conductivity, significant aspect ratio, and adaptability in assembly techniques, positioning them at the forefront of TC research [5]. Efforts to optimize AgNW films have involved innovative material improvements and diverse assembly methods, including ultrasonic spraying, rod coating, and dip coating. In our previous work, AgNWs and MXene were combined

Published online: 18 September 2024

to form flexible films for EMI shielding and heating performance [6]. However, balancing high conductivity with optimal light transmittance continues to be a challenge in AgNW film development.

Two improvements were focused on AgNW films: (1) reducing the junction resistance of AgNW networks and (2) creating more optical transmittance channels. The application of transparent coatings, such as rGo [7], MXene [8, 9], and PEDOT: PSS layers [10], significantly reduces the films' contact resistance. Gao utilized ultrasonic spraying to create a nested structure of AgNW grids, enhancing the optoelectronic performance of TCs through the vertical stacking of AgNWs while ensuring sufficient optical channels [11]. Another method to enhance optical performance involves utilizing the self-assembly capability of AgNWs or templating methods to establish patterned AgNW networks. Xiong utilized the coffee-ring effect during droplet evaporation to drive the AgNWs at the droplet peripheries, thus forming AgNW rings [12]. Yang employed a mechanical templating method to precisely modulate the morphology of AgNWs [13].

Patterned AgNW films concentrate light channels in specific areas, significantly optimizing light transmission efficiency. This approach increases the proportion of light channels across the film, thereby aggregating the distribution of optical transparency windows and improving the visible light transmittance [14]. Conversely, random networks exhibit scattered light channels, leading to an inconsistent distribution of light transmittance and constraining enhancements in optical performance [15]. Previous research leveraging AgNWs' self-assembly characteristics typically resulted in ring-shaped or microchannel patterns adhering to the substrate [16]. These configurations, while increasing light channels, fail to preserve effective electron migration pathways and require the use of costly, eco-adverse techniques like photolithography and chemical etching for templating [17].

While ring-patterned AgNW films maintain high light transmittance, their electron pathways are notably limited, restricted to the pathways within their ringed configurations, potentially limiting electron transport efficiency. Hence, by guaranteeing elevated transparency, the enhancement of electron pathways can substantially amplify the benefits associated with self-assembly structural configurations [18, 19].

Therefore, we introduce a technique based on a biotemplate (tomato epidermis), transferring the morphology of tomato epidermal cells onto a polyethylene naphthalate (PEN) substrate via a straightforward mechanical pressing approach [20]. Subsequently, the application of ultrasonic spraying initiates a self-assembly process, resulting in the formation of "island-like" AgNW clusters by morphological constraints. This structure differs from traditional ring patterns by offering a greater relative proportion of light channels across the total film area. Simultaneously, this innovative structure provides varied and abundant pathways for electron migration, facilitating free electron movement in a multidimensional space and thus markedly improving electron dynamics [21]. Such advancements are crucial for optoelectronic devices, including touch screens, displays, and solar cells, which depend on high light transmittance for optimal performance and efficiency [22]. Furthermore, utilizing bio-template has three advantages: (1) It can generate complex and precise micro-scale structures, challenging to achieve with traditional chemical or physical techniques. (2) They are renewable and biodegradable. (3) It can offer a high degree of customizability, allowing for the adjustment and optimization of templates to produce the desired specific structures and shapes. This strategy paves the way for biomimetic design, replicating structures and functions observed in nature, and propelling the creation of innovative materials and technologies.

Herein, the flexible transparent films named "A-TEP" exhibiting "island-like'' AgNW clusters were fabricated, featuring concentrated optical channels that result in a transmittance of 99.9% at 550 nm. For enhanced electrical properties, a layer of random AgNW network was sprayed on the foundational AgNW clusters, creating a composite CRS (bottomed cluster and topped random structure) architecture. This innovation film named "A-TEP" with CRS boasts excellent optoelectronic properties that can be applied in EMI shielding and electronic heating fields.

2 Experimental section

2.1 Materials

The materials used encompassed silver nanowires (AgNWs), polyethylene naphthalate (PEN), sodium dodecyl sulfate (SDS), isopropanol (IPA), and anhydrous ethanol (AE). AgNWs (10 mg/mL) with 25–30 nm diameter and 10–30 μm length were obtained from Zhejiang Kechuang Advanced Materials Technology Co., Ltd (Zhejiang, China). Tomatoes for the experiment were acquired from a local supermarket.

2.2 Fabrication of TEP

The TEP fabrication process involved carefully removing a section of tomato skin using tweezers, immersing it in a 10% SDS solution, and subjecting it to ultrasonication at 450 W for 12 min to remove surplus tomato pulp, achieving decellularized tomato skin. This skin was then dried at 80 ℃ in ambient conditions, placed between two pristine PEN sheets, and subjected to a 4-h mechanical press at 3 MPa. The PEN replicated

from the tomato skin's outer side was termed TEP, which, upon microscopic analysis, revealed distinct cell wall patterns.

2.3 Ultrasonic spraying AgNWs

The initial layer of AgNWs was applied via ultrasonic spraying with a 0.32 mg/mL AgNW-ethanol solution at room temperature. Adjusting the spray flow, droplets were tailored to match TEP's cellular dimensions, creating "island-like" clusters through the interaction of AgNW droplets with the TEP substrate. A second layer of AgNW random network was then added to improve the film's electrical performance. For subsequent layers, a 0.25 mg/mL AgNW solution in a mixture of deionized water and IPA (1:5:5) was sprayed at 100 °C, 0.1 mL/min flow rate, fine-tuning the number of applications to optimize AgNW coverage for superior optoelectronic properties. Following the spraying process, the AgNW film was soaked in a 10% NaCl solution for 25 s, subsequently washed with fresh water, and dried, resulting in the final AgNW films.

2.4 Characterization

Optical surface morphology and surface roughness were captured using a light microscope (Nikon, Japan, LV-UEPI) and a white light three-dimensional optical microscope (Veeo Contour GT-K1). X-ray diffraction analysis of crystalline structures and focused configurations was performed with a MiniFlex600 Desktop X-ray diffractometer (XRD, Japan). Surface morphology and microstructural details were further investigated using a scanning electron microscope (SEM, Thermofisher Verios 460 + EDX, America), an atomic force microscope (AFM, HORIBA, OmegaScope, Japan), and a transmission electron microscope (TEM, Fei, Tecnai f20, America). Chemical bonds were analyzed through Fourier transform infrared spectroscopy (FTIR, Bruker, VERTEX70, Germany) and X-ray photoelectron spectroscopy (XPS, Thermo Scientific, K-alpha, America). Transmittance data, using a blank PEN substrate for auto-zeroing, was obtained with an UV–visible-infrared spectrometer (UV–Vis-IR, PerkinElmer, Lambda 40750S, America).

The EMI SE of films in the 8.2–12.4 GHz range (X-band) was assessed using the vector network analyzer (VNA, Agilent, PNA-N5234A, America) with the waveguide technique, featuring a window size of 22.86 × 10.16 mm. The comprehensive analysis includes calculations for total shielding effectiveness (SE_T), shielding effectiveness due to reflection (SE_R), absorption (SE_A), and the overall shielding efficiency (%) as follows:

$$R = |S11|^2 = |S22|^2 \tag{1}$$

$$T = |S21|^2 = |S12|^2 \tag{2}$$

$$T + A + R = 1 \tag{3}$$

$$SE_R = -10\log(1 - R) \tag{4}$$

$$SE_A = -10\log(T/(1 - R)) \tag{5}$$

$$SE_T = SE_A + SE_R \tag{6}$$

Additionally, the electromagnetic interference (EMI) shielding efficiency (%), which reflects the proportion of electromagnetic waves (EMWs) obstructed by the shielding material, is calculated using the formula:

$$Shieldingefficiency(\%) = 100 - \left(1/10^{SE/10}\right) \times 100 \tag{7}$$

A FOTRIC infrared thermal camera from China was utilized to observe and document temperature variations on the surface of the film. The film was sectioned into 3 × 3 cm squares, with rectangular silver electrodes about 0.5 cm wide applied to both sides through vacuum thermal evaporation. These electrodes were connected to an external power supply with conductive silver paste and copper foil. To capture temperature changes, the infrared camera focused on the reverse side of the AgNW surface, leveraging the substrate's superior heat retention properties. The methodology for temperature measurement and the associated formulas for the film are detailed below:

$$T_{equ} = T_0 + U^2/RAh \tag{8}$$

$$P = UI/A \tag{9}$$

Here, T_0 denotes the initial temperature, U represents the input drive voltage, R is the resistance across the copper electrodes, A signifies the surface area, h is the total heat transfer coefficient, and I is the current flowing between electrodes when a drive voltage is applied.

3 Results and discussion

3.1 Fabrication and characterization of AgNWs-TEP

Transparent AgNW films were synthesized on patterned PEN substrates, following a detailed methodology illustrated in Fig. 1. The initial template utilized for patterning was sourced from fresh tomato epidermis, as depicted in Fig. 1a, characterized by its microscale cellular architecture [23]. SEM revealed cell walls offering substantial structural support, with the spaces between cells collapsing inward. After decellularization with a 10% sodium dodecyl sulfate (SDS) solution as shown in Fig. 1b, a tomato cytoskeleton was formed [24]. Placing it as a template on PEN and applying

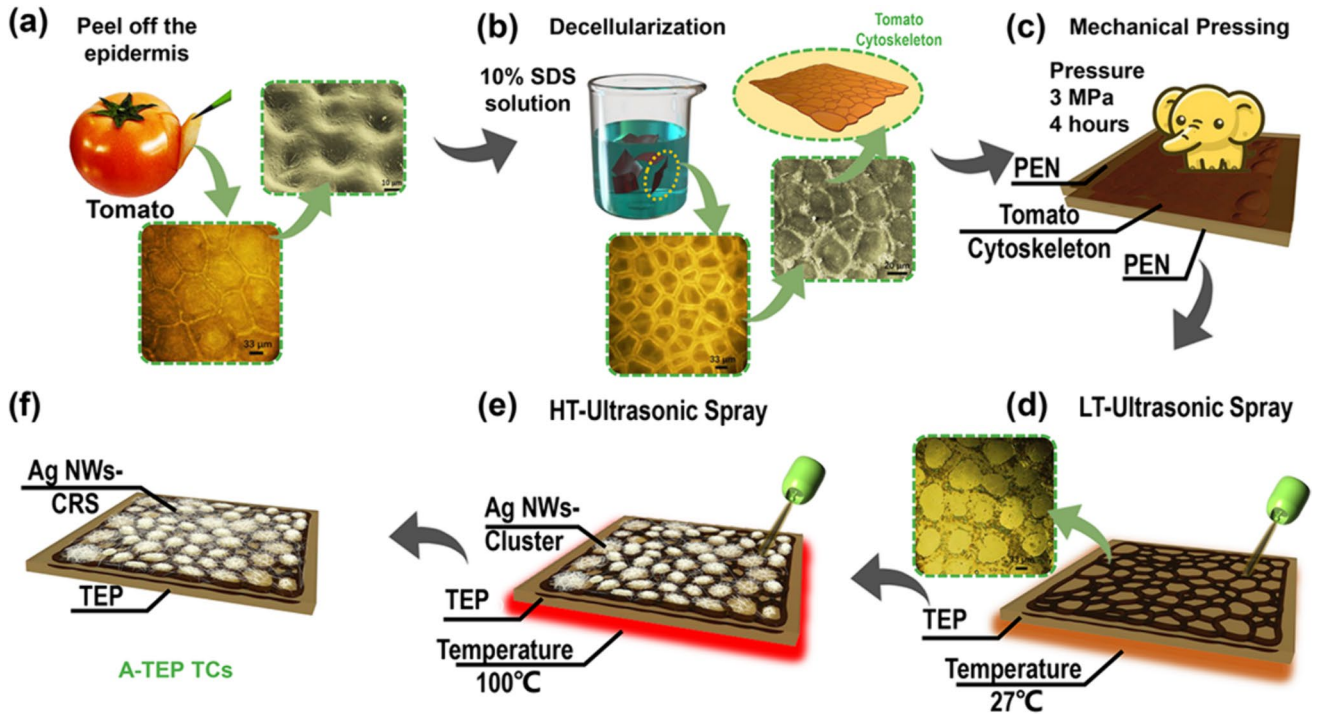

Fig. 1 Preparation process of transparent AgNW films with bottomed "island-like" AgNW cluster and topped random network structure. **a** Fresh tomato epidermis, **b** decellularized tomato cytoskeleton, **c** mechanically pressed tomato epidermis PEN (TEP), **d** low-temperature ultrasonic sparing of bottomed "island-like" AgNW cluster layer, **e** high-temperature ultrasonic sparing of topped random AgNW network layer, **f** A-TEP film with CRS

mechanical pressing at 3 MPa for 4 h as seen in Fig. 1c transferred the tomato cytoskeleton to PEN, referred to as TEP (tomato epidermis morphology on PEN). The successfully fabricated TEP is displayed in Fig. 1d, with low-temperature (27 °C) ultrasonic spraying creating "island-like" AgNW clusters. Low temperature is utilized to mitigate the rate of evaporation, thereby facilitating the stable liquid droplet configurations on the substrate, in order to facilitate "island-like" structural formation. For further improvement of electrical properties, high-temperature (100 °C) ultrasonic spraying (Fig. 1e) was employed to apply a random AgNW network as a covering layer and bridge the gaps between AgNW inter-clusters. Ultimately, this resulted in (Fig. 1f) AgNW-TEP films (A-TEP) with bottomed AgNW clusters and topped AgNW random network structure (CRS).

AgNWs are presented in Fig. 2a with XRD diffraction patterns showcasing distinct peaks that correspond to the (111), (200), (220), and (311) planes. Figure 2b depicts a high-resolution HRTEM image of an individual AgNW, both verifying the high crystallinity structure [25]. The FTIR spectroscopy in Fig. 2c reveals transmittance peaks at 3448 cm^{-1} and 1610 cm^{-1}, corresponding to O–H and C = O bonds, respectively, which are critical for the stability and functionality of the AgNW film. The absorption peak around 2900 cm^{-1} is related to C-H bond stretching, typically from organic stabilizers like PVP used in the AgNW synthesis [26]. A comprehensive XPS analysis in Fig. 2d reveals prominent peaks correlating with the core levels of Ag 3d (368.1 eV), O 1 s (531.1 eV), and C 1 s (284.6 eV). The high-resolution XPS spectrum of AgNWs in Fig. 2e, detailing the doublet peaks of Ag $3d_{5/2}$ (367.4 eV) and Ag $3d_{3/2}$ (373.4 eV), is consistent with the characteristic peak positions of metallic silver. Fig. 2f shows the high-resolution XPS spectrum of O 1 s, indicating the presence of a small amount of silver oxide and surface-adsorbed hydroxyl groups.

AgNW-ethanol solution (0.31 mg/mL) was ultrasonically sprayed onto PEN and TEP substrates at varying flow (0.21–0.25 mL/min) under identical ambient conditions, resulting in distinct patterns of deposition. Sheet resistance measurements, as shown in Fig. 3a, indicate that on PEN substrates, AgNW films exhibit reduced sheet resistance with increased spray flow, due to the enhanced droplet size and density [27]. On TEP substrates, however, the sheet resistance follows an unusual pattern of decrease-increase–decrease as spray flow rises. Figure 3b, c displays the differences in surface roughness between PEN and TEP, where TEP's arithmetic average roughness (R_a = 0.0256 µm) surpasses that of PEN (R_a = 0.0234 µm). The water contact angles presented in Fig. 3d indicate an improvement in

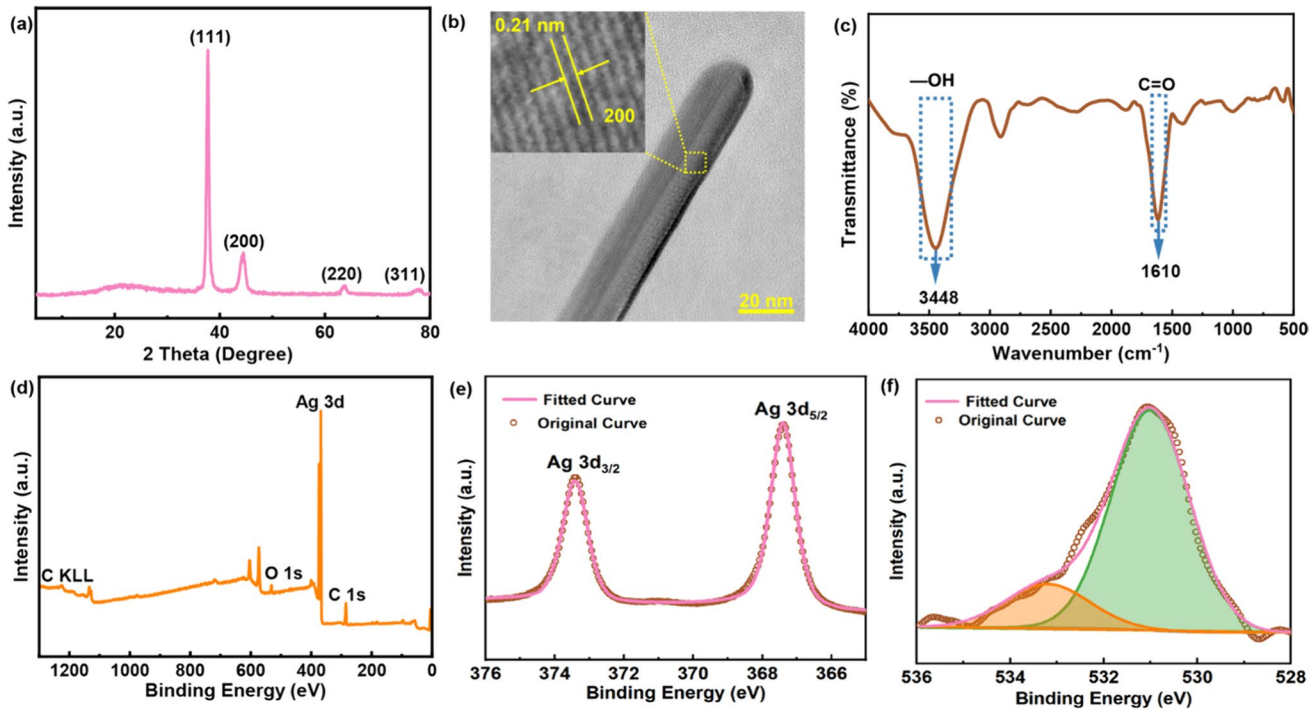

Fig. 2 **a** XRD diffraction patterns of AgNWs, **b** HRTEM image of AgNWs, **c** the FTIR spectroscopy of AgNWs, **d** full spectrum XPS analysis of AgNWs, **e** high-resolution XPS spectrum of Ag 3d, **f** and O 1 s

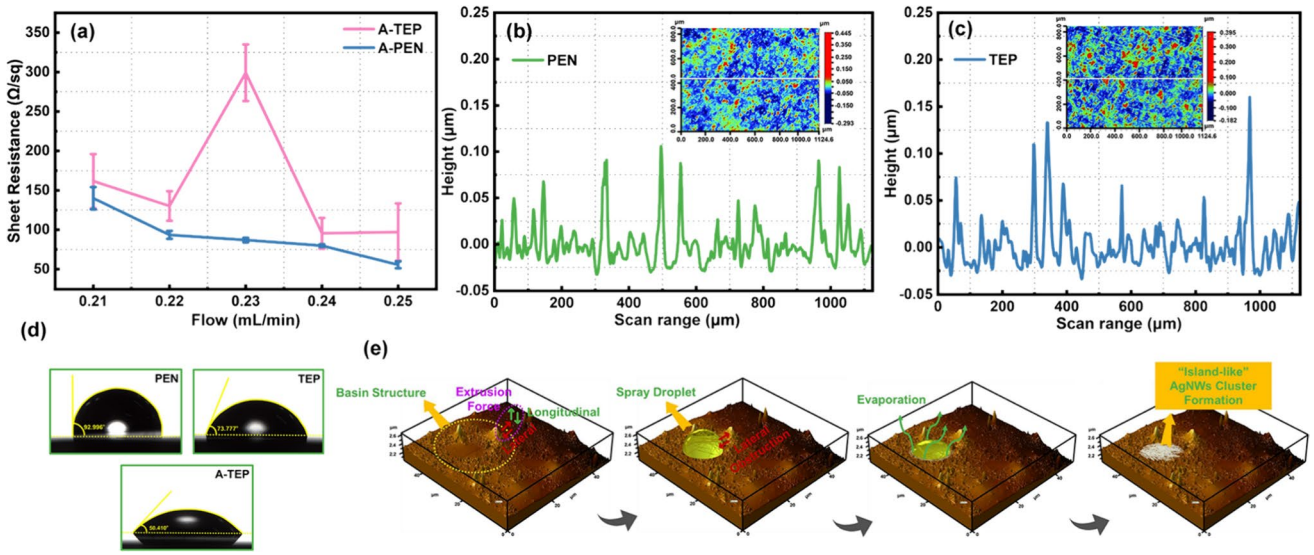

Fig. 3 **a** Sheet resistance of AgNW films on PEN and TEP substrates with varying spray flow, **b** arithmetic average roughness of PEN substrate, **c** arithmetic average roughness of TEP substrate, **d** water contact angle of the PEN, TEP substrate, and A-TEP film, **e** schematic illustration of "island-like" AgNW cluster on TEP substrate

hydrophilicity with an increase in substrate roughness from a macroscopic perspective (Fig. S1, Supplementary Information: roughness and water contact angle), influenced by the compression of rough fibers from the cellular cytoskeleton [28]. The evaporation dynamics of AgNW droplets on TEP are illustrated in Fig. 3e. The texture on TEP transferred by tomato cytoskeletons exhibits an irregular and rough morphology, creating separated basin structures that prevent the merging of droplets between adjacent basins. Additionally, the intercellular areas display smooth basin morphologies,

leading to droplet aggregation in these parts, supported by the surrounding protuberances. When the droplets formed by the spraying flow precisely exhibit the aforementioned dynamic behavior, isolated AgNW clusters are produced, resulting in a sudden increase in sheet resistance at a flow rate of 0.23 mL/min. As the size and density of the droplets continue to increase (0.24 mL/min), a bundle of connections forms between the AgNW clusters, leading to a decrease in sheet resistance.

In pursuit of elucidating the reasons for the pronounced variation in sheet resistance observed at the flow rates of 0.23–0.24 mL/min, a comprehensive morphological characterization was undertaken. Fig. 4 illustrates that spray flow variations lead to distinct AgNW morphologies on PEN and TEP substrates, differentiated by their surface roughness and tension [29]. AgNWs form a uniform random network without notable features on the PEN substrate (Fig. 4a–e). In contrast, on TEP, the interplay between AgNW drop and microstructures of TEP leads to the formation of AgNW clusters upon the selection of suitable droplet densities and dimensions (Fig. 4 h). As the dimensions and density of the droplets expand to match the micro-morphological characteristics of the substrate, which facilitates the AgNW clusters' connectivity and separation, resulting in well-defined, interconnected clusters (Fig. 4i). At spray flows ranging from 0.21 to 0.22 mL/min, droplet size remains minimal, allowing for smaller droplets to uniformly attach across both smooth basins and rugged textures on the TEP, creating a random network appearance (Fig. 4f, g). With an increase in flow to 0.23–0.24 mL/min, the spray droplets' size and density gather specifically at the center of smooth basins, resulting in the formation of distinctive "island" structures (Fig. 4 h, i). Advancing the spray flow to 0.25 mL/min amplifies the droplets' size and density to submerge the TEP's structure, culminating in a random network (Fig. 4j). This dynamic behavior of droplets throughout the spraying process is instrumental in developing unique "island-like" AgNW clusters.

Figure 5a–c displays an overview and detailed SEM images of "island-like" AgNW clusters, with each cluster approximately 40 µm in diameter. Adjacent clusters are linked by AgNW bundles, consisting of tens of longitudinally interconnected AgNWs, each about 15 µm long. A detailed AFM view of an AgNWs cluster's edge in Fig. 5d reveals densely woven AgNW aggregations accompanied by an empty PEN area. Such concentrated clustering boosts light channel density, thus improving the film's optical qualities. However, considerable junction resistance and absent electrical paths inter-clusters diminish the film's electrical properties. Therefore, to enhance electron transit between clusters, a top-layered random AgNW network covers the clusters. Figure 5e, f shows the overview and detailed SEM images of AgNW clusters covered by a random network structure (CRS), with the dense network effectively bridging inter-cluster gaps. This approach significantly reduces sheet resistance, maintaining excellent optical attributes.

3.2 Optical transmittance and sheet resistance

The process of coverage of AgNW random networks over AgNW clusters and the subsequent changes in the films' sheet resistance are depicted in Fig. 6. Fig. 6a illustrates the process of overlaying a single layer of random network on AgNW clusters. "R1 (PEN)" acts as the control, representing the random AgNW film applied to PEN substrates. "CR1" describes adding a single random network layer to the "C (TEP)" film, while "NaCl CR1" signifies the NaCl solution treatment. Initially, the "C (TEP)" film demonstrates an

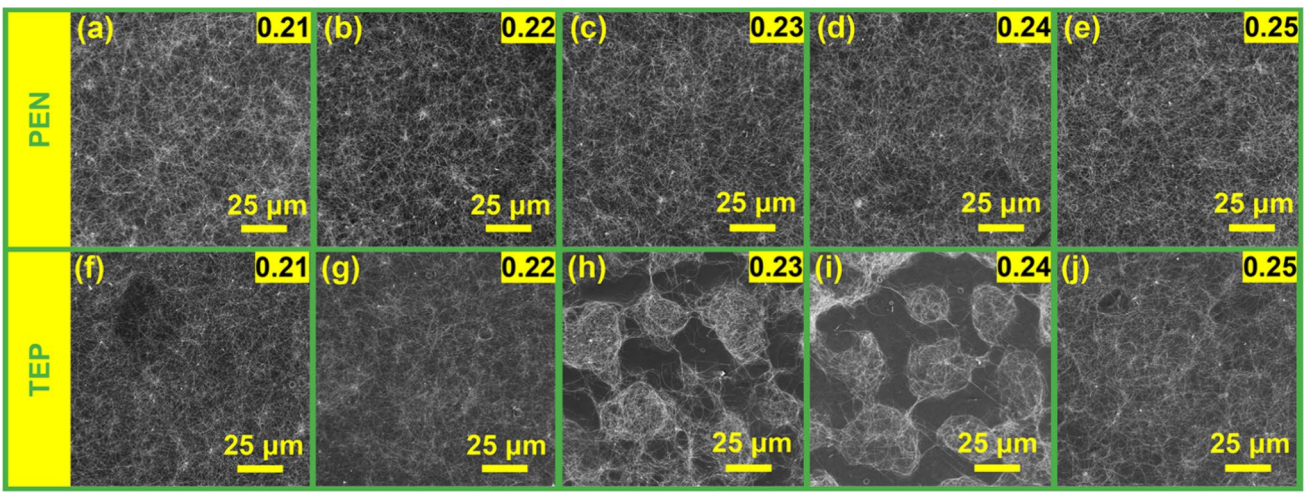

Fig. 4 **a** – **e** SEM images of AgNWs on PEN substrate with varying spray flow, **f** – **j** SEM images of AgNWs on TEP substrate with varying spray flow

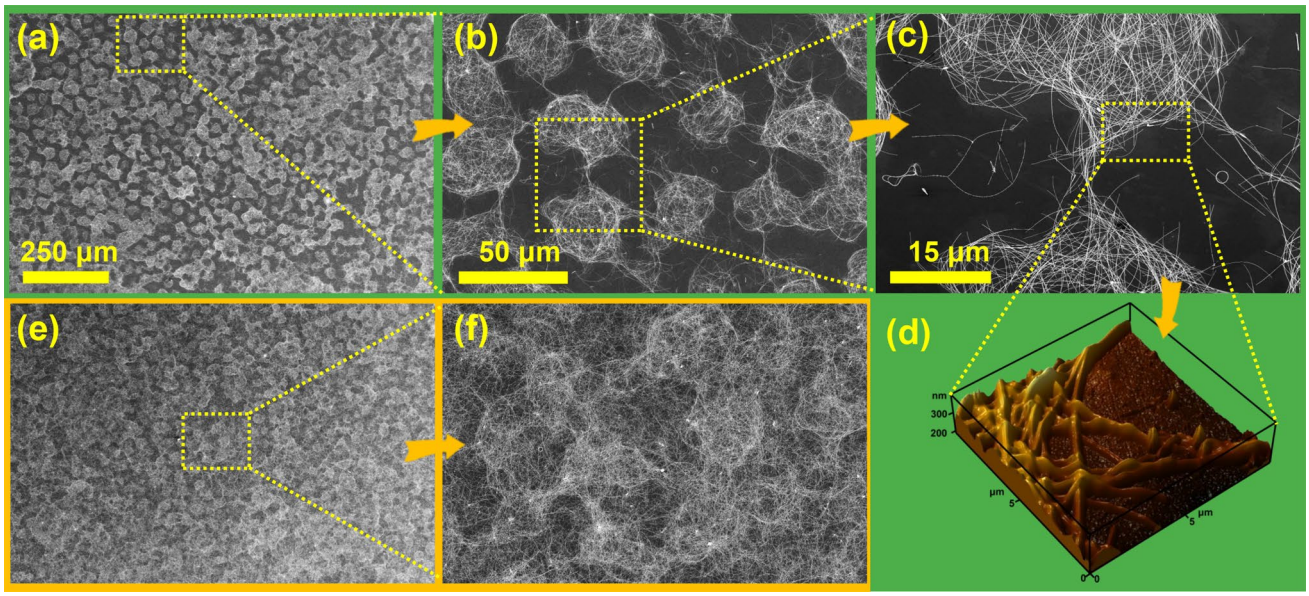

Fig. 5 **a** – **c** Overview and detailed SEM images of "island-like" AgNW clusters, **d** AFM image of the edges of AgNW cluster, **e** , **f** overall and detailed SEM images of AgNW clusters covered by random AgNW networks

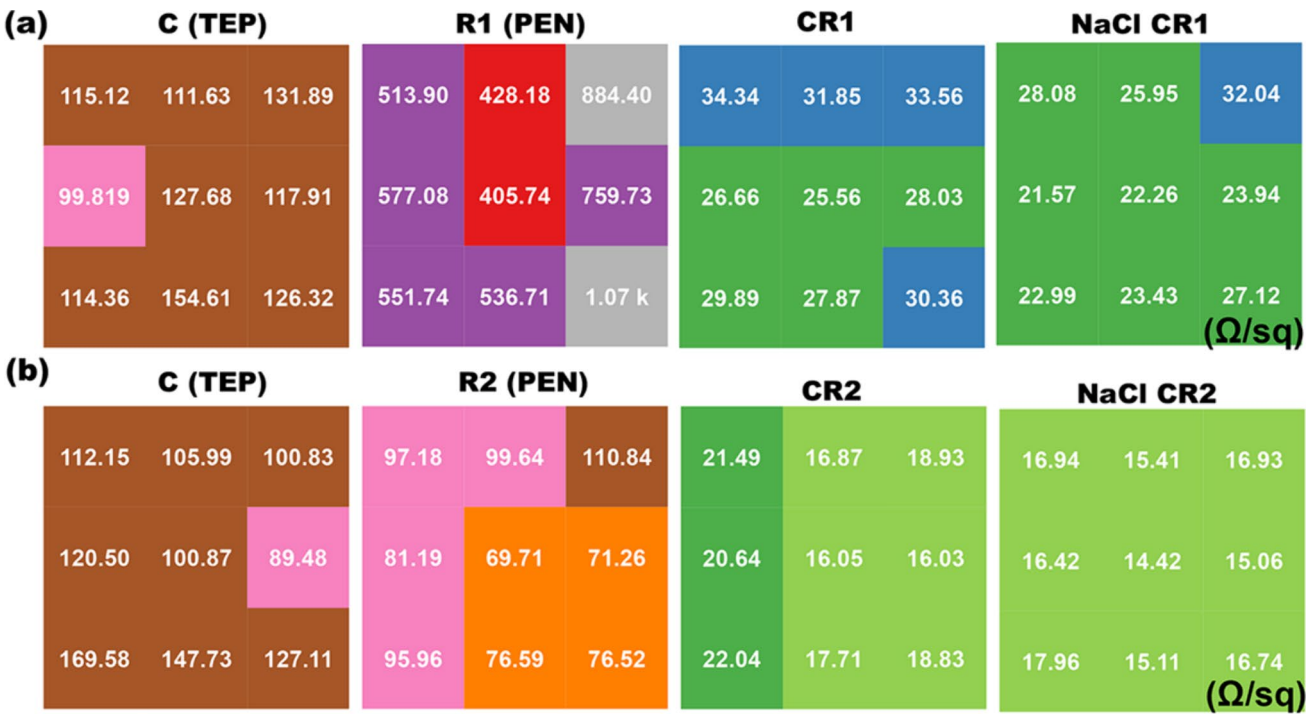

Fig. 6 Resistance optimization process for "island-like" AgNW clusters. **a** Coated with a layer of random AgNW networks and subjected to NaCl treatment, **b** coated with two layers of random AgNW networks and subjected to NaCl treatment

uneven resistance distribution, following the addition of one layer of the AgNW random network. The random AgNW network fills the gaps between isolated islands with conductive pathways, thereby significantly enhancing the electron transport efficiency between the islands, which can notably reduce the "CR1" film's sheet resistance from 121.63 to 29.79 Ω/sq. Subsequent NaCl treatment, which exposes Ag^+ on the surface, effectively welds the contacting AgNWs, further lowering the resistance to 25.26 Ω/sq [30–34]. As illustrated in Fig. 6b, overlaying AgNW clusters with two

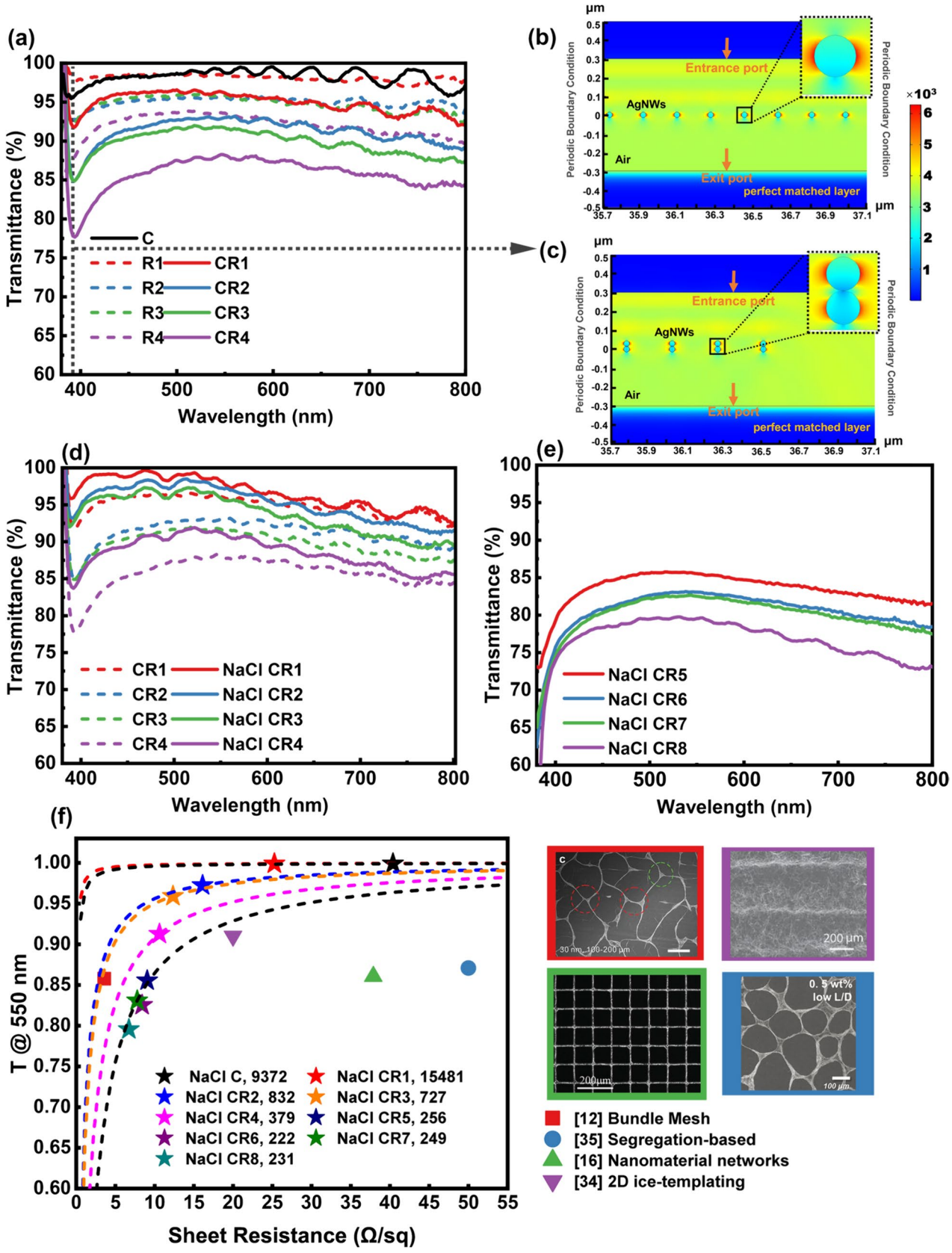
(a)
Transmittance (%)
Wavelength (nm)
C
R1
CR1
R2
CR2
R3
CR3
R4
CR4
(b)
μm
Periodic Boundary Condition
Entrance port
AgNWs
Air
Exit port
perfect matched layer
×10³
(c)
(d)
CR1
NaCl CR1
CR2
NaCl CR2
CR3
NaCl CR3
CR4
NaCl CR4
(e)
NaCl CR5
NaCl CR6
NaCl CR7
NaCl CR8
(f)
T @ 550 nm
Sheet Resistance (Ω/sq)
NaCl C, 9372
NaCl CR1, 15481
NaCl CR2, 832
NaCl CR3, 727
NaCl CR4, 379
NaCl CR5, 256
NaCl CR6, 222
NaCl CR7, 249
NaCl CR8, 231
200 μm
0.5 wt%
low L/D
[12] Bundle Mesh
[35] Segregation-based
[16] Nanomaterial networks
[34] 2D ice-templating

◂**Fig. 7** **a** Transmittance variation with coverage of random AgNW networks compared to pure random AgNW networks, **b** simulated electric field diagram of random AgNW network, **c** simulated electric field diagram of "island-like" AgNW clusters, **d** transmittance variation after NaCl treatment, **e** transmittance corresponding to different spray coating layers, **f** relationship between sheet resistance and transmittance @550 nm under different spray coatings compared with other AgNW-assembled research

layers of random networks leads to a sharp reduction in the "C (TEP)" film from 119.36 to 16.11 Ω/sq. As the layers in the random AgNW networks increase, the electron pathways also increase, leading to a decrease in sheet resistance. However, this also results in increased parasitic absorption of light, adversely affecting the transparency of the film. Continuing to overlay the "C (TEP)" film with several layers of AgNW network, the complete process of resistance changes is listed in Fig. S2 (Supplementary Information: Resistance optimization process).

Fig. 7 elucidates the impact of coverage variation and post-treatment on the optical and electrical properties of AgNW films. In Fig. 7a, the comparison of transmittance among C film on TEP, CRS film, and R film on PEN shows that the transmittance of the CRS film decreases with increased layers of AgNW random network. C film exhibits a stronger plasmonic resonance effect at 390 nm compared to the random AgNW networks (R film) [35]. To elucidate the factors contributing to the changes in the absorption peak observed at 390 nm, detailed modeling was executed for comprehensive understanding. The established modeling by adjusting only the spatial arrangement of AgNWs within a fixed total quantity. Simulation results shown in Fig. 7b exhibit a minor absorption peak at 390 nm in the random network's transmittance curve (R), attributed to the resonant absorption of surface plasmon dipole moments generated by the longitudinal cross-section of AgNWs. The enhanced resonant absorption observed in Fig. 7c is likely due to stronger plasmonic coupling between closely stacked AgNWs. This clustering amplifies the local electromagnetic fields, leading to a more pronounced absorption peak (Supplementary Information: simulation model schematic and design, Fig. S4, 5). Post-NaCl treatment significantly improves transmittance across all films, maintaining it above 90% as shown in Fig. 7d. The NaCl solution can reconfigure silver nanowires (Fig. S3), decrease aggregation for improved film uniformity, and promote the etching away of oxidized layers, thereby potentially enhancing the AgNWs' conductivity and transparency [36]. Subsequent layers of AgNW random network, detailed in Fig. 7e, sustain transmittance above 79.55% at 550 nm. The critical relationship between sheet resistance and optical transmittance at 550 nm, depicted in Fig. 7f, employs the figure of merit (FoM) for comprehensive optoelectronic performance evaluation [37]. (Supplementary Information: Formula S1) The island-like AgNW clusters (NaCl C) demonstrated a supremely high FoM of 9372, attributed to its high transparency to visible light. Covering with a first layer of random networks (NaCl CR1) slightly affected the light transmittance of the island-like shape but significantly reduced sheet resistance to 40% of its original value, causing a remarkable enhancement in the FoM to 15,481. With the continuous addition of random layers, the FoM value gradually decreased to about 250 and remained stable. Compared with other patterned AgNW self-assembled films, this work has an incomparable advantage in optoelectronic performance due to the synchronized concentration on light and electron channels [38–49].

3.3 EMI shielding performance

Figure 8a showcases the X-band EMI shielding effectiveness (SE) for AgNW films with "island-like" clusters under different layers of random networks. Post NaCl treatment, Ag^+ ions on AgNW surfaces effectively weld the junctions, boosting conductivity and EMI shielding by enriching electron transport pathways [50]. The "NaCl C" film exhibits a 14.07 dB EMI SE, blocking 96.09% of electromagnetic waves (EMWs). This is due to the impedance mismatch, leading primarily to wave reflection rather than penetration into the AgNWs' intricate network [51]. Adding one layer of random AgNW networks fills the inter-cluster gaps, raising the EMI SE to 20.04 dB, hence blocking 99.01% of EMWs and achieving commercial-grade performance of 20 dB [52]. Figure 8b reveals that the reflection loss (SE_R), driven by the films' high conductivity, escalates with additional AgNW network layers, enhancing the barrier against EMW penetration [53]. Achieving a 4-layer AgNW configuration, the sample NaCl CR4 showcases an SE of 26.27 dB, effectively obstructing 99.76% of EMWs. This enhancement primarily results from ohmic loss, induced by free electron collisions within the multiple reflections between AgNW network with incident EMWs, leading to notable absorption loss (SE_A) [54, 55]. Figure 8c displays the reflection (R), transmission (T), and absorption (A) coefficients, highlighting that R significantly exceeds T and A. With an increase in layers, the rise of the R coefficient indicates that reflection is the dominant shielding mechanism for AgNW films, closely associated with conductivity [56]. Figure 8d, e demonstrates that overlaying AgNWs with random networks gradually enhances electromagnetic shielding, achieving a peak SE of 29.68 dB in the sample NaCl CR8 of this CRS system. This configuration effectively blocks 99.89% of EMWs, showcasing exceptional shielding performance. Comparing Fig. 8a–e, as the coverage of AgNW random network increases, the sheet resistance decreases, and the EMI SE value gradually reaches a threshold, which is limited by the

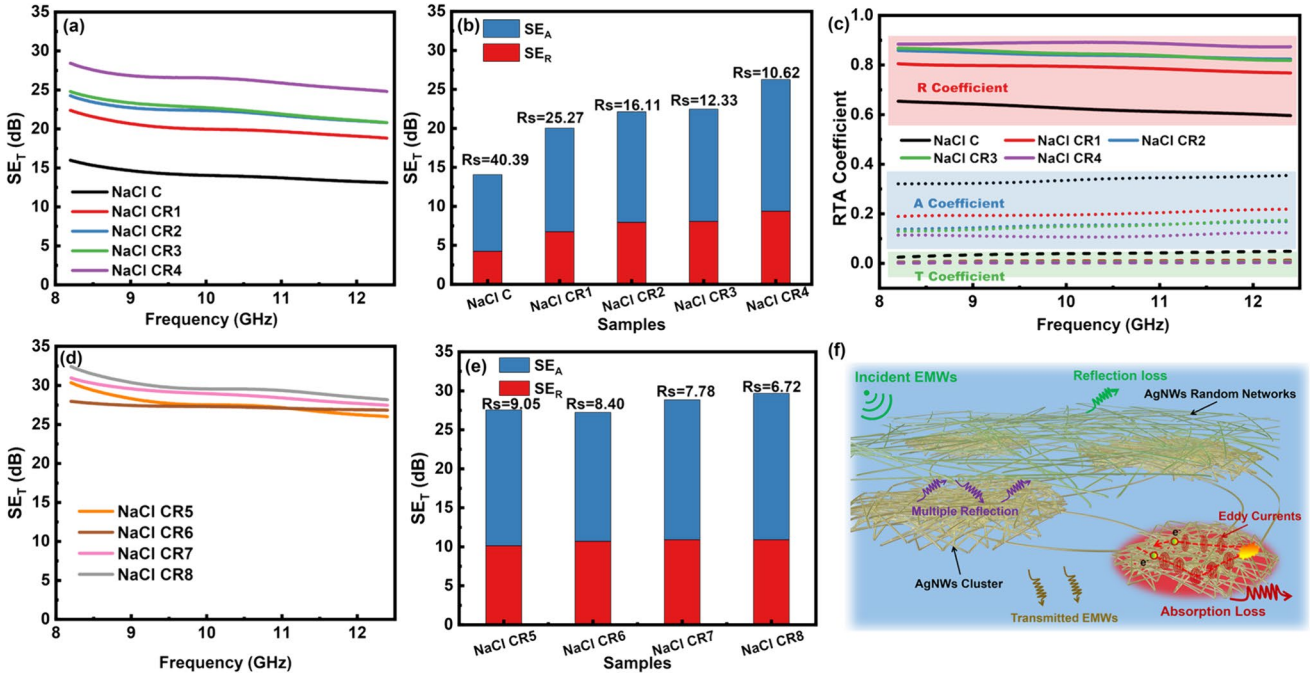

Fig. 8 EMI SE A , SE R , and SE T of C films with different spray coatings. **a** Relationship between frequency and X-band SE T with 1–4 layers, **b** bar chart of SE A and SE R with 1–4 layers, **c** the R, T, A coefficient 1–4 layers, **d** relationship between frequency and X-band SE T with 5–8 layers, **e** bar chart of SE A and SE R with 5–8 layers, **f** schematic illustration of the electromagnetic interference shielding mechanism of CRS films

singular contribution of silver's high conductivity to electromagnetic energy loss.

Figure 8f depicts the electromagnetic interference (EMI) shielding mechanism in CRS AgNW films, featuring a dual-layer design with "island-like" clusters at the bottom and a random AgNW network on top. Incident EMW first encounter and are predominantly reflected by the random network, incurring SE_R. The waves that penetrate films engage in extensive interactions within the dense conductive mesh, including multiple reflections and collisions with free electrons, which generate eddy currents and ohmic loss. The closed-loop configurations within clusters facilitate uninterrupted electron movement, amplifying SE_A. Moreover, the CRS films' elaborate architecture mirrors a resistance-inductance-capacitance (RLC) circuit, based on the transmission line theory [57]. This design efficiently absorbs and transforms incoming electromagnetic waves (EMWs) into alternate forms of energy, predominantly thermal energy.

Figure 9 showcases the visual transparency comparison of a blank PEN sample to A-TEP films with CR structure. The visual transparency is not significantly affected by the

Fig. 9 The visual transparency comparison of "island-like" AgNW films covered with varying numbers of random AgNW network layers to blank PEN

bio-template strategy; the films ensure exceptional light transmittance in the visible light spectrum while achieving effective electromagnetic shielding performance.

Figure 10 compares the electromagnetic shielding performance and optical transmittance of this study with other AgNW-based research. Due to the unique clustering and vertical stacking of random networks, the concentrated distribution of light channels enables CRS AgNW films to achieve exceptionally high optical transmittance while ensuring good electromagnetic shielding performance [58–61].

3.4 Joule heating performance

Based on Joule's Law ($Q = U^2 \cdot R^{-1} \cdot t$), where U stands for the external drive voltage, R for the resistance between the electrodes of the film, and t denotes the operating time [62]. Figure 11a shows the NaCl CR4 film's temperature–time response at different voltages, with a sheet resistance of 10.62 Ω/sq. With the drive voltage increasing from 2.0 to 5.5 V, the saturation temperature rises from 52.8 to 170.0 ℃, and the film exhibits a swift response time of around 50 s. Figure 11b shows the NaCl CR8 film's response, with a lower sheet resistance of 6.72 Ω/sq, peaking at 170.8 ℃ under lower drive at 4.0 V and a faster response time of about 38 s. As the drive voltage increases from 3.5 to 4.0 V, the NaCl CR8 film exhibits more significant fluctuations and spikes in the heating curve. When the temperature reaches the maximum tolerance of PEN (150 ℃), rapid temperature changes cause thermal deformation of the substrate, resulting in fluctuations in the saturation temperature. Consequently, this causes localized heating instability in the AgNWs, ultimately resulting in their fracture. Comparing Fig. 11a, b, at the same driving voltage range (2.0–4.0 V), the NaCl CR8 film exhibits a higher heating saturation temperature and quicker response, suggesting more heat is generated with lower sheet resistance at equivalent drive voltages. Figure 11c captures the saturation current of NaCl CR4 and NaCl CR8 films at changing drive voltages, showing that NaCl CR8 film's inter-electrode resistance remains below NaCl CR4's and increases gradually with the rise in heating temperature [63]. Figure 11d illustrates the NaCl CR8 film's temperature response to steadily increasing voltages, highlighting the heater's operational stability across a range of voltages. Finally, Fig. 11e details 100 cyclic reheating tests on the NaCl CR8 film at 3.0 V, confirming its reliability and environmental stability as a heater [64].

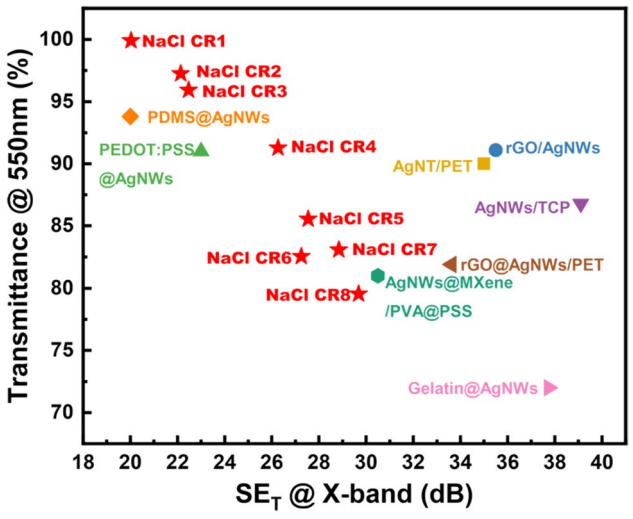

Fig. 10 Comparison of X-band SE_T and transmittance @550 nm with other research

Fig. 12a demonstrates remarkable thermal homogeneity, achieving a uniform temperature during the heating process. Remarkably, this uniformity is still retained even under bending (Fig. S6), evidencing the film's substantial capability as a flexible heater in dynamic conditions [65]. Figure 12b presents the oxidative stability of NaCl CR4 and NaCl CR8 films under atmospheric conditions across 33 days. The NaCl CR4 film exhibits an increasing trend in sheet resistance, with a relative change ($(\Delta R/R_0) \times 100\%$, ΔR is the change in resistance, R_0 is the initial resistance.) reaching 55% by day 33, reflecting its vulnerability to oxidation. Conversely, the NaCl CR8 film shows enhanced oxidation resistance, with only a 20% relative change in resistance at the end of the observation period, suggesting a higher resistance to oxidation.

4 Conclusion

Utilizing a bio-template approach combined with a two-step ultrasonic spray method, transparent conductive films with a dual-layer structure were developed for applications in EMI shielding and Joule heating. This dual-layer structure features a bottomed layer of "island-like" AgNW clusters and a topped layer of random AgNW networks (CRS). The AgNW cluster layer displays a unique "island-like" morphology, attributed to the employment of a tomato epidermis PEN (TEP) template, which features microscale cellular frameworks. This morphology differs from conventional self-assembled AgNW structures by centralizing light channels, simultaneously facilitating multi-dimensional electron transport routes. This unique morphology simultaneously concentrates light and electron channels, exhibiting an extremely high FoM value of 9372. The integration of the topped AgNW network layer ensures optimal linkage among clusters, thus amplifying the optoelectronic characteristics. Substantially enhanced electrical properties without compromising optical transmittance led to a remarkable FoM value of 15,481, accompanied by an EMI SE of 20.04 dB, satisfying commercial requirements. The TEP template, derived

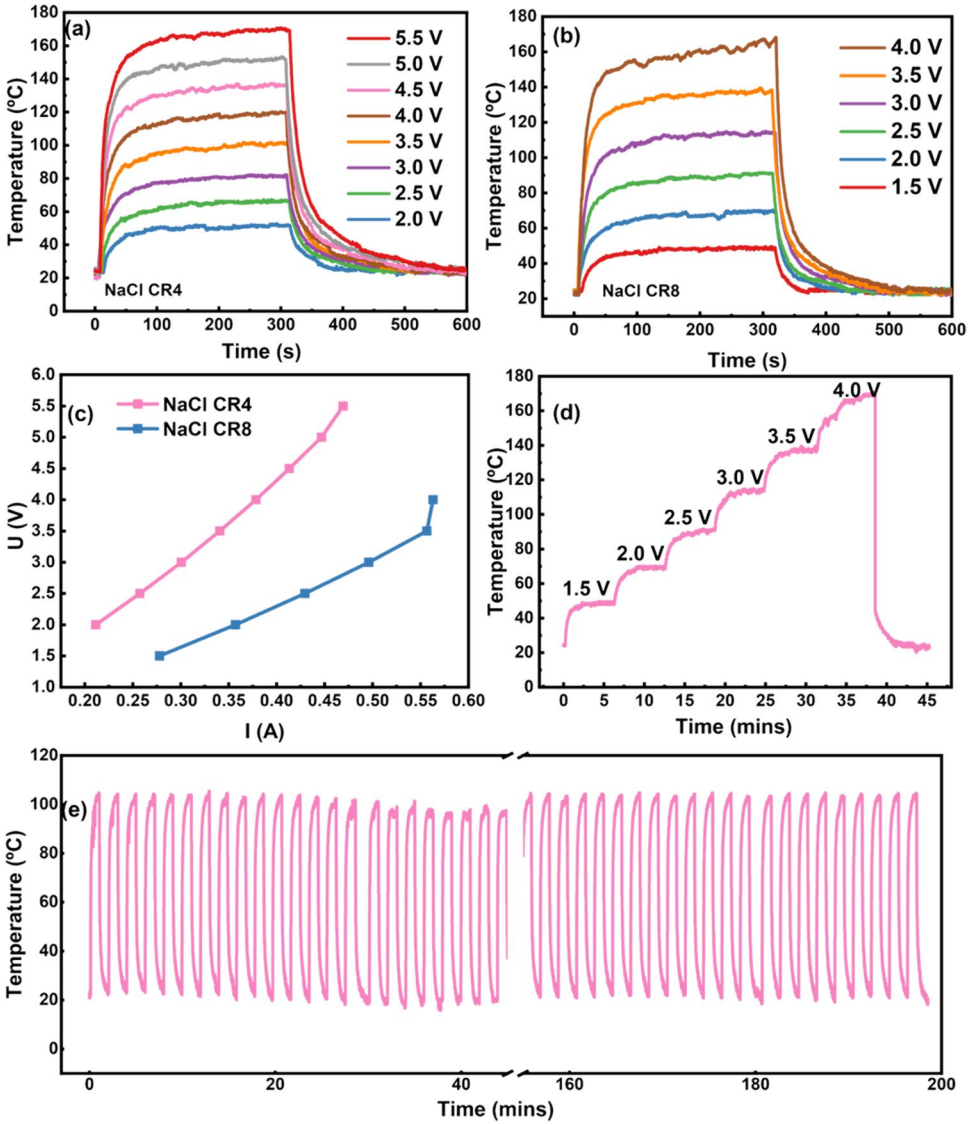

Fig. 11 **a** Time–temperature response curves of NaCl CR4 film under different driving voltages, **b** time–temperature response curves of NaCl CR8 film under different driving voltages, **c** relationship between driving voltage and saturation current for different AgNW films, **d** temperature–time curves of NaCl CR8 film under successive varying voltages, **e** repeated heating curves of NaCl CR8 film at a driving voltage of 3.0 V

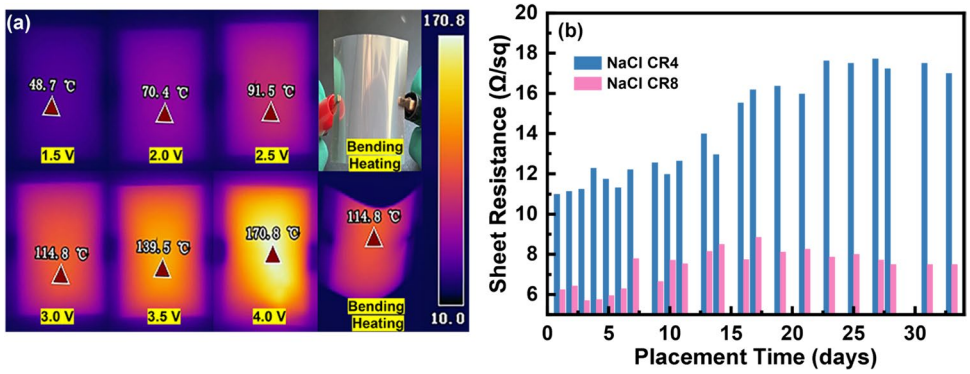

Fig. 12 **a** Uniform heating performance and flexibility demonstration of the NaCl CR8 film heater, **b** stability of sheet resistance under atmospheric conditions of NaCl CR4 and NaCl CR8 film

from tomato epidermis through a mechanical pressing technique, exemplifies a novel paradigm in AgNW self-assembly, characterized by its simplicity, environmental benignity, and structural precision. Exhibiting tunable optoelectronic performance within the visible light (T@550 nm = 91.26%, Rs = 10.62 Ω/sq; T@550 nm = 79.54%, Rs = 6.72 Ω/sq), these films are appropriate for transparent EMI shielding and heating applications. It demonstrates EMI SE of 26.28

dB and 29.68 dB, respectively, and maintains a steady high heating temperature of 170.8 °C at a 4.0 V driving voltage. The films hold the potential for transparent heating windows against electromagnetic interference, facilitating defrosting and defogging, or serving as an effective photonic absorbent conductive layer integrated with photovoltaic devices.

Supplementary Information The online version contains supplementary material available at https://doi.org/10.1007/s42114-024-00957-9.

Acknowledgements The authors would like to thank all the foundation supports listed in the funding parts.

Author contributions Zhongmei Xia: Conceptualization (lead); Visualization (equal); Writing – original draft (lead). Longlong Tian: Writing – original draft (equal); Methodology (lead); Resources (lead). Tianyi Zhang: Methodology (lead); Resources (lead). Bin Tian: Methodology (lead); Resources (lead). Fuhua Hou: Funding acquisition (equal); Visualization (lead). Ashraf Y. Elnaggar: Review and Discussion. Salah M. El-Bahy: Review and Discussion. Xiaojing Wang: Writing—review & editing, Discussion, Conceptualization. Yanlai Wang: Funding acquisition (equal); Visualization (lead). Tiantian Li: Conceptualization (lead); Funding acquisition (lead); Visualization (lead); Visualization (lead). Zeinhom M. El-Bahy: English grammer and valuable discussion.

Funding This work was supported by the National Natural Science Foundation of China (Grant Nos. 62164009, 62264012), the Inner Mongolia University Research Foundation for Advanced Talents (Nos. 21200–5175162 (2017), 10000–21311201/005 (2021)), the Inner Mongolia Autonomous Region for Advanced Talents in 2020 (No. 12000–12102628), the Inner Mongolia Higher Education Research Project (No. NJZZ22343), and the Natural Science Foundation of Inner Mongolia (No.2022MS05042). The authors were also supported by the Taif University, Saudi Arabia, through project number (TU-DSPP-2024–76).

Data availability No datasets were generated or analysed during the current study.

Declarations

Ethical approval Experiments in this paper do not involve any vivo testing on animal subjects, human subjects, or human tissue.

Conflict of interest The authors declare that they have no known competing financial interests or personal relationships that could have appeared to influence the work reported in this paper.

References

1. De Volder MFL, Tawfick SH, Baughman RH, Hart AJ (2013) Carbon nanotubes: present and future commercial applications. Science 339:535–539. https://doi.org/10.1126/science.1222453
2. Kim Y, Hyeong SK, Choi Y, Lee SK, Lee JH, Yu HK (2021) Transparent and flexible electromagnetic interference shielding film using ITO nanobranches by internal scattering. ACS Appl Mater Interfaces 13:61413–61421. https://doi.org/10.1021/acsami.1c17967
3. Xu JD, Li RS, Ji SR, Zhao BC, Cui TR, Tan XC, Gou GY, Jian JM, Xu HK, Qiao YC, Yang Y, Zhang S, Ren TL (2021) Multifunctional graphene microstructures inspired by honeycomb for ultrahigh performance electromagnetic interference shielding and wearable applications. ACS Nano 15:8907–8918. https://doi.org/10.1021/acsnano.1c01552
4. Weng GM, Li J, Alhabeb M, Karpovich C, Wang H, Lipton J, Maleski K, Kong J, Shaulsky E, Elimelech M, Gogotsi Y, Taylor AD (2018) Layer-by-layer assembly of cross-functional semi-transparent mxene-carbon nanotubes composite films for next-generation electromagnetic interference shielding. Adv Funct Mater 28:1803360. https://doi.org/10.1002/adfm.201803360
5. Zhang N, Wang Z, Song R, Wang Q, Chen H, Zhang B, Lv H, Wu Z, He D (2019) Flexible and transparent graphene/silver-nanowires composite film for high electromagnetic interference shielding effectiveness. Sci Bull 64:540–546. https://doi.org/10.1016/j.scib.2019.03.028
6. Xia ZM, Zhang TY, Tian LL, Tian B, Ni J, Hou FH, Li TT (2024) Flexible MXene hybrid films with a tuned silver nanowire framework for electromagnetic interference shielding and ultralow voltage-driven joule heating. ACS Appl Nano Mater 7:3748–3760. https://doi.org/10.1021/acsanm.3c05342
7. Yang Y, Chen S, Li W, Li P, Ma JG, Li BS, Zhao XN, Ju ZS, Chang HC, Xiao L, Xu HY, Liu YC (2020) Reduced graphene oxide conformally wrapped silver nanowire networks for flexible transparent heating and electromagnetic interference shielding. ACS Nano 14:8754–8765. https://doi.org/10.1021/acsnano.0c03337
8. Jin M, Chen W, Liu LX, Zhang HB, Ye L, Min P, Yu ZZ (2022) Transparent, conductive and flexible MXene grid/silver nanowire hierarchical films for high-performance electromagnetic interference shielding. J Mater Chem A 10:14364. https://doi.org/10.1039/d2ta03689d
9. Chen W, Liu LX, Zhang HB, Yu ZZ (2020) Flexible, transparent, and conductive $Ti_3C_2T_x$ mxene−silver nanowire films with smart acoustic sensitivity for high-performance electromagnetic interference shielding. ACS Nano 14:16643–16653. https://doi.org/10.1021/acsnano.0c01635
10. Hosseini E, Sabet N, Arjmand M, Sundararaj U, Hassanzadeh H, Zarifi MH, Karan K (2022) Multilayer polymeric nanocomposite thin film heater and electromagnetic interference shield. Chem Eng J 435:134598. https://doi.org/10.1016/j.cej.2022.134598
11. Gao S, Zhao X, Fu Q, Zhang T, Zhu J, Hou F, Ni J, Zhu C, Li T, Wang Y, Murugadoss V, Mersal GAM, Ibrahim MM, El-Bahy ZM, Huang M, Guo Z (2022) Highly transmitted silver nanowires-SWCNTs conductive flexible film by nested density structure and aluminum-doped zinc oxide capping layer for flexible amorphous silicon solar cells. J Mate Sci Technol 126:152–160. https://doi.org/10.1016/j.jmst.2022.03.012
12. Xiong J, Li S, Ciou JH, Chen J, Gao D, Wang J, Lee PS (2021) A tailorable spray-assembly strategy of silver nanowires bundle mesh for transferable high-performance transparent conductor. Adv Funct Mater 31:2006120. https://doi.org/10.1002/adfm.202006120
13. Yang BR, Cao W, Liu GS, Chen HJ, Noh YY, Minari T, Hsiao HC, Lee CY, Shieh HPD, Liu C (2015) Microchannel wetting for controllable patterning and alignment of silver nanowire with high resolution. ACS Appl Mater Interfaces 7:21433–21441. https://doi.org/10.1021/acsami.5b06370
14. Chen Y, Carmichael RS, Carmichael TB (2019) Patterned, flexible, and stretchable silver nanowire/polymer composite films as transparent conductive electrodes. ACS App Mater Interfaces 11:31210–31219. https://doi.org/10.1021/acsami.9b11149
15. Kang S, Kim T, Cho S, Lee Y, Choe A, Walker B, Ko SJ, Kim JY, Ko H (2015) Capillary printing of highly aligned silver nanowire transparent electrodes for high-performance optoelectronic devices. Nano Lett 15:7933–7942. https://doi.org/10.1021/acs.nanolett.5b03019

16. Su Z, Yu HSC, Zhang X, Brugger J, Zhang H (2019) Liquid assembly of floating nanomaterial sheets for transparent electronics. Adv Mater Technol 4:1900398. https://doi.org/10.1002/admt.201900398
17. Lin Y, Yuan W, Ding C, Chen S, Su W, Hu H, Cui Z, Li F (2020) Facile and efficient patterning method for silver nanowires and its application to stretchable electroluminescent displays. ACS Appl Mater Interfaces 12:24074–24085. https://doi.org/10.1021/acsami.9b21755
18. Guan P, Zhu R, Zhu Y, Chen F, Wan T, Xu Z, Joshi R, Han Z, Hu L, Wu T, Lu Y, Chu D (2022) Performance degradation and mitigation strategies of silver nanowire networks: a review. Crit Rev Solid State Mater Sci 47:435–459. https://doi.org/10.1080/10408436.2021.1941753
19. Du H, Wan T, Qu B, Cao F, Lin Q, Chen N, Lin X, Chu D (2017) Engineering silver nanowire networks: from transparent electrodes to resistive switching devices. ACS Appl Mater Interfaces 9:20762–20770. https://doi.org/10.1021/acsami.7b04839
20. Wang CY, Jiao K, Yan JF, Wan MC, Wan QQ, Breschi L, Chen JH, Tay FR, Niu LN (2021) Biological and synthetic template-directed syntheses of mineralized hybrid and inorganic materials. Prog Mater Sci 116:100712. https://doi.org/10.1016/j.pmatsci.2020.100712
21. Cui J, Ren X, Mei X, Fan Z, Huang C, Wang Z, Sun X, Wang W (2023) Morphological characteristics and atomic evolution behavior of nanojoints in Ag nanowire interconnect network. Int J Extrem Manuf 5:025503. https://doi.org/10.1088/2631-7990/acc434
22. Chen X, Chen B, Jiang B, Gao T, Shang G, Han ST, Kuo CC, Roy VAL, Zhou Y (2023) Nanowires for UV–vis–IR optoelectronic synaptic devices. Adv Funct Mater 33:2208807. https://doi.org/10.1002/adfm.202208807
23. Bai H, Xie B, Wang Z, Li M, Sun P, Wei S, Wang W, Wu H, Bai L, Li J (2021) Application of the tissue-engineered plant scaffold as a vascular patch. ACS Omega 6:11595–11601. https://doi.org/10.1021/acsomeg
24. Cheng YW, Shiwarski DJ, Ball RL, Whitehead KA, Feinberg AW (2020) Engineering aligned skeletal muscle tissue using decellularized plant-derived scaffolds. ACS Biomater Sci Eng 11:3046–3054. https://doi.org/10.1021/acsbiomaterials.0c00058
25. Nian Q, Saei M, Xu Y, Sabyasachi G, Deng B, Chen YP, Cheng GJ (2015) Crystalline nanojoining silver nanowire percolated networks on flexible substrate. ACS Nano 9:10018–10031. https://doi.org/10.1021/acsnano.5b03601
26. Koczkur KM, Mourdikoudis S, Polavarapu L, Skrabalak SE (2015) Polyvinylpyrrolidone (PVP) in nanoparticle synthesis. Dalton Trans 44:17883–17905. https://doi.org/10.1039/c5dt02964c
27. Wang G, Zhao Y, Yang F, Zhang Y, Zhou M, Ji G (2022) Multifunctional integrated transparent film for efficient electromagnetic protection. Nano-Micro Lett 14:65. https://doi.org/10.1007/s40820-022-00810-y
28. Kim H-J, Kim D-E (2012) Effect of surface roughness of top cover layer on the efficiency of dye-sensitized solar cell. Sol Energy 86:2049–2055. https://doi.org/10.1016/j.solener.2012.04.007
29. Yang SB, Choi H, Lee DS, Choi CG, Choi SY, Kim ID (2015) Improved optical sintering efficiency at the contacts of silver nanowires encapsulated by a graphene layer. Small 11:1293–1300. https://doi.org/10.1002/smll.201402474
30. Yang SB, Choi H, Lee DS, Choi CG, Choi SY, Kim ID (2018) Preparation of smooth, flexible and stable silver nanowires - polyurethane composite transparent conductive films by transfer method. Mater Res Express 5:059501. https://doi.org/10.1088/2053-1591/aac0e3
31. Onuralp C, Doga D, Murathan C, Ogeday CM, Onur D, Sahin C, Emrah UH (2024) Post-treatment optimization for silver nanowire networks in transparent droplet-based TENG sensors. Nano Energy 128:109940. https://doi.org/10.1016/j.nanoen.2024.109940
32. Du MY, Yang Z, Miao YQ, Wang C, Dong P, Wang H, Guo K (2024) Facile nanowelding process for silver nanowire electrodes toward high-performance large-area flexible organic light-emitting diodes. Adv Funct Mater 2404567. https://doi.org/10.1002/adfm.202404567
33. Bian MX, Qian YC, Cao HQ, Huang TT, Ren ZX, Dai XD, Zhang SF, Qiu Y, Si RM, Yang LY, Yin SG (2023) Chemically welding silver nanowires toward transferable and flexible transparent electrodes in heaters and double-sided perovskite solar cells. ACS Appl Mater Interfaces 15:13307–13318. https://doi.org/10.1021/acsami.2c21996
34. Liu WC, Prentice Joseph CA, Patrick CE, Watt AAR (2024) Enhancing conductivity of silver nanowire networks through surface engineering using bidentate rigid ligands. ACS Appl Mater Interfaces 16:4150–4159. https://doi.org/10.1021/acsami.3c15207
35. Kim J, Ampadu EK, Choi WJ, Oh E (2019) Photocurrent spectra from PbS photovoltaic infrared detectors using silver nanowires as plasmonic nano antenna electrodes. Nanotechnology 30:075201. https://doi.org/10.1088/1361-6528/aaf194
36. Hyungseok K, Yeontae K, Siuk C, Gi-Ra Yi, Jeong HC (2017) Halide welding for silver nanowire network electrode. ACS Appl Mater Interfaces 9:30779–30758. https://doi.org/10.1021/acsaelm.3c00484
37. De S, King PJ, Lyons PE et al (2010) Size effects and the problem with percolation in nanostructured transparent conductors. ACS Nano 4:7064–7072. https://doi.org/10.1021/nn1025803
38. Han J, Yang J, Gao W et al (2021) Ice-templated, large-area silver nanowire pattern for flexible transparent electrode. Adv Funct Mater 31:2010155. https://doi.org/10.1002/adfm.202010155
39. Shin JW, Lim HR, Cho HB et al (2021) Segregation-controlled self-assembly of silver nanowire networks using a template-free solution-based process. Nanoscale 13:8442. https://doi.org/10.1039/d0nr08762a
40. Cao XL, Lan D, Zhang Y, Jia ZR, Wu GL, Yin PF (2023) Construction of three-dimensional conductive network and heterogeneous interfaces via different ratio for tunable microwave absorption. Adv Compos Hybrid Ma 6:187. https://doi.org/10.1007/s42114-023-00763-9
41. Jia ZR, Liu JK, Gao ZG, Zhang CH, Wu GL (2024) Molecular intercalation-induced two-phase evolution engineering of 1T and 2H-MS_2 (M = Mo, V, W) for interface-polarization-enhanced electromagnetic absorbers. Adv Funct Mater 34:2405523. https://doi.org/10.1002/adfm.202405523
42. Wu NN, Zhao BB, Lian YY, Liu SS, Xian Y, Gu JW, Wu GL (2024) Metal organic frameworks derived Ni_xSe_y@NC hollow microspheres with modifiable composition and broadband microwave attenuation. Carbon 226:119215. https://doi.org/10.1016/j.carbon.2024.119215
43. Zhang QL, Lan D, Deng SL, Gu JW, Wang YQ, Ren JW, Wu GL, Jia ZR (2024) Constructing multiple heterogeneous interfaces in one-dimensional carbon fiber materials for superior electromagnetic wave absorption. Carbon 226:119233. https://doi.org/10.1016/j.carbon.2024.119233
44. Hao ZW, Zhou J, Lin SN, Lan D, Li HY, Wang H, Liu D, Gu JW, Wang XB, Wu GL (2024) Customized heterostructure of transition metal carbides as high-efficiency and anti-corrosion electromagnetic absorbers. Carbon 228:119323. https://doi.org/10.1016/j.carbon.2024.119323
45. Dong YH, Lan D, Xu S, Gu JW, Jia ZR, Wu GL (2024) Controllable fiberization engineering of cobalt anchored mesoporous hollow carbon spheres for positive feedback to electromagnetic wave absorption. Carbon 228:119339. https://doi.org/10.1016/j.carbon.2024.119339

46. Chen XL, Lan D, Zhou LT, Zeng Z, Liu YK, Du SX, Zou ZY, Wu GL (2024) Rational construction of $ZnFe_2O_4$ decorated hollow carbon cloth towards effective electromagnetic wave absorption. Ceram Int 50:24549–24557. https://doi.org/10.1016/j.ceramint.2024.04.190
47. Guo ZG, Lan D, Ren XY, Jia ZR, Wu GL (2024) Manipulating cellulose-based dual-network coordination for enhanced electromagnetic wave absorption in magnetic porous carbon nanocomposites. Compos Commun 48:101922. https://doi.org/10.1016/j.coco.2024.101922
48. Li JJ, Lan D, Cheng YH, Jia ZR, Liu PB, Shi XT, Guo H, Feng AL, Wu GL, Yin PF (2024) Constructing mixed-dimensional lightweight magnetic cobalt-based composites heterostructures: an effective strategy to achieve boosted microwave absorption and self-anticorrosion. J Mater Sci Technol 196:60–70. https://doi.org/10.1016/j.jmst.2024.02.016
49. Zhou JX, Huang XM, Lan D, Cheng YH, Xue FY, Jia CY, Wu GL, Jia ZR (2024) Polymorphic cerium-based Prussian blue derivatives with in situ growing CNT/Co heterojunctions for enhanced microwave absorption via polarization and magnetization. Nano Res 17(3):2050–2060. https://doi.org/10.1007/s12274-023-6216-7
50. James TH (1939) The reduction of silver ions by hydroquinone. J Am Chem Soc 61:648–652
51. Chen Q, Huang L, Wang X, Yuan Y (2023) Transparent and flexible composite films with excellent electromagnetic interference shielding and thermal insulating performance. ACS Appl Mater Interfaces 15:24901–24912. https://doi.org/10.1021/acsami.3c03140
52. Liang C, Gu Z, Zhang Y, Ma Z, Qiu H, Gu J (2021) Structural design strategies of polymer matrix composites for electromagnetic interference shielding: a review. Nano-Micro Lett 13:181. https://doi.org/10.1007/s40820-021-00707-2
53. Zhu M, Yan X, Li X, Dai L, Guo J, Lei Y, Xu Y, Xu H (2022) Flexible, transparent, and hazy composite cellulosic film with interconnected silver nanowire networks for EMI shielding and joule heating. ACS Appl Mater Interfaces 14:45697–45706. https://doi.org/10.1021/acsami.2c13035
54. Wen C, Li X, Zhang R, Xu C, You W, Liu Z, Zhao B, Che R (2022) High-density anisotropy magnetism enhanced microwave absorption performance in $Ti_3C_2T_x$ MXene@Ni microspheres. ACS Nano 16:1150–1159. https://doi.org/10.1021/acsnano.1c08957
55. Zhao B, Bai Z, Lv H, Yan Z, Du Y, Guo X, Zhang J, Wu L, Deng J, Zhang DW, Che R (2023) Self-healing liquid metal magnetic hydrogels for smart feedback sensors and high-performance electromagnetic shielding. Nano-Micro Lett 15:79. https://doi.org/10.1007/s40820-023-01043-3
56. Sun K, Wang F, Yang W, Liu H, Pan C, Guo Z, Liu C, Shen C (2021) Flexible conductive polyimide fiber/mxene composite film for electromagnetic interference shielding and joule heating with excellent harsh environment tolerance. ACS Appl Mater Interfaces 13:50368–50380. https://doi.org/10.1021/acsami.1c15467
57. Celozzi S, Araneo R, Lovat G (2008) Electromagnetic shielding. Shielding effectiveness of stratified media. Wiley, Hoboken, pp 48–51
58. Jiang C, Tan D, Li Q, Huang J, Bu J, Zang L, Ji R, Bi S, Guo Q (2021) High-performance and reliable silver nanotube networks for efficient and large-scale transparent electromagnetic interference shielding. ACS Appl Mater Interfaces 13:15525–15535. https://doi.org/10.1021/acsami.1c00590
59. Jung J, Lee H, Ha I, Cho H, Kim KK, Kwon J, Won P, Hong S, Ko SH (2017) Highly stretchable and transparent electromagnetic interference shielding film based on silver nanowire percolation network for wearable electronics applications. ACS Appl Mater Interfaces 9:44609–44616. https://doi.org/10.1021/acsami.7b14626
60. Wang G, Hao L, Zhang X, Tan S, Zhou M, Gu W, Ji G (2022) Flexible and transparent silver nanowires/biopolymer film for high-efficient electromagnetic interference shielding. J Colloid Interface Sci 607:89–99. https://doi.org/10.1016/j.jcis.2021.08.190
61. Liu J, Zhang Y, Cheng W, Lei S, Song L, Wang B, Hu Y (2022) Anti-fogging, frost-resistant transparent and flexible silver nanowire $Ti_3C_2T_x$ MXene based composite films for excellent electromagnetic interference shielding ability. J Colloid Interface Sci 608:2493–2504. https://doi.org/10.1016/j.jcis.2021.10.171
62. Hong S, Lee H, Lee J, Kwon J, Han S, Suh YD, Cho H, Shin J, Yeo J, Ko SH (2015) Highly stretchable and transparent metal nanowire heater for wearable electronics applications. Adv Mater 27:4744–4751. https://doi.org/10.1002/adma.201500917
63. Ma Z, Xiang X, Shao L, Zhang Y, Gu J (2022) Multifunctional wearable silver nanowire decorated leather nanocomposites for joule heating, electromagnetic interference shielding and piezoresistive sensing. Angew Chem Int Ed 61:e202200705. https://doi.org/10.1002/anie.202200705
64. Ma Z, Kang S, Ma J, Shao L, Wei A, Liang C, Gu J, Yang B, Dong D, Wei L, Ji Z (2019) High-performance and rapid-response electrical heaters based on ultraflexible, heat-resistant, and mechanically strong aramid nanofiber/Ag nanowire nanocomposite papers. ACS Nano 13:7578–7590. https://doi.org/10.1021/acsnano.9b00434
65. Zhang D, Yin R, Zheng Y, Li Q, Liu H, Liu C, Shen C (2022) Multifunctional MXene/CNTs based flexible electronic textile with excellent strain sensing, electromagnetic interference shielding and Joule heating performances. Chem Eng J 438:135587. https://doi.org/10.1016/j.cej.2022.135587